Effects of alkali metal intercalation on structural and electronic properties of molybdenum disulfide

Mádai, Eszter; Anusuyadevi, Prasaanth Ravi; Gonugunta, Prasad; Mohseni Armaki, A.; Mol, Arjan; Taheri, Peyman; Hartkamp, Remco

DOI
10.1016/j.apsusc.2025.164284

Publication date
2025

Document Version
Final published version

Published in
Applied Surface Science

Citation (APA)
Mádai, E., Anusuyadevi, P. R., Gonugunta, P., Mohseni Armaki, A., Mol, A., Taheri, P., & Hartkamp, R. (2025). Effects of alkali metal intercalation on structural and electronic properties of molybdenum disulfide. *Applied Surface Science*, *714*, Article 164284. https://doi.org/10.1016/j.apsusc.2025.164284

Applied Surface Science 714 (2025) 164284

Contents lists available at ScienceDirect

Applied Surface Science

journal homepage: www.elsevier.com/locate/apsusc

Full length article

Effects of alkali metal intercalation on structural and electronic properties of molybdenum disulfide

Eszter Mádai [a], Prasaanth Ravi Anusuyadevi [a], Prasad Gonugunta [a], Amirhossein Mohseni Armaki [a], Arjan Mol [a], Peyman Taheri [a], Remco Hartkamp [b,*]

[a] Department of Materials Science and Engineering, Faculty of Mechanical Engineering, Delft University of Technology, Mekelweg 2, Delft, 2628 CD, South-Holland, The Netherlands

[b] Department of Process and Energy, Faculty of Mechanical Engineering, Delft University of Technology, Leegwaterstraat 39, Delft, 2628 CB, South-Holland, The Netherlands

ARTICLE INFO

Keywords:
Molybdenum disulfide
Intercalation
Hydration shell
Electronic properties
Phase transition

ABSTRACT

2D materials, characterized by their extensive surface area and customizable chemical and electronic properties, offer compelling advantages as advanced materials. These unique attributes pave the way for the development of next-generation electronics and optoelectronics, photo- and electro-catalysis, energy storage and conversion devices, and sensors. The most prominent and commonly available 2D transition metal dichalcogenide, molybdenum disulfide (MoS_2), has already shown its potential for advanced applications. However, its relatively unfavorable electronic structure and limited intrinsic conductivity lower its suitability for applications that require high conductivity, such as electrocatalysts. One way to enhance its conductivity is by electrochemically intercalating alkali metal ions, e.g., Na^+ and K^+, into its layered structure, potentially adjusting its electronic structure. Here, we present a comprehensive investigation into the atomic-scale intercalation mechanism using molecular dynamics simulations, complemented by experimental analysis of structural and electronic properties at the macro scale through various characterization techniques. It is demonstrated that the hydration shell of ions serves as an energy barrier to intercalation as it undergoes a structural change during the intercalation. When alkali metal ions are intercalated into MoS_2, they introduce more defects and enhance conductivity. Notably, these effects are more pronounced for potassium than for sodium.

1. Introduction

Meeting today's technological and societal needs relies on advanced materials whose properties can be precisely tailored for high performance and demanding applications. A prominent and widely researched group of advanced materials is the family of 2D materials, due to their superior mechanical, electronic, and structural properties [1]. The high surface-to-bulk ratio of 2D structures enhances their surface functionality, while their layered architecture allows for precise tuning of chemical and electronic properties [2]. These materials find applications across a wide range of fields, including electronics and optoelectronics (e.g., semiconductors, photodetectors), photo-, electro- (e.g., water purification, electrolyzers for water splitting, CO_2 reduction) [3] and thermal catalysis [4], energy storage and conversion (e.g., batteries, supercapacitors) [5,6], field emitters [7] and sensing (e.g., gas and biosensors) [8,9].

2D materials encompass a diverse range of classes, including transition metal dichalcogenides (TMDs), MXenes, graphene and its derivatives, hexagonal boron nitride (h-BN), and layered metal oxides, each offering distinct structural and electronic properties tailored for various applications [10]. Recently, 2D transition metal borides (MBenes) have also emerged as a promising class of 2D materials, exhibiting notable electrochemical and catalytic properties [11]. As a member of the (TMD) family, MoS_2 is an abundant and cost-effective material that offers a tunable chemistry and bandgap, excellent chemical stability, and a layered structure, making it a promising choice for advanced applications [12].

A monolayer of MoS_2 consists of a layer of molybdenum (Mo) atoms sandwiched between two layers of sulfur (S) atoms. These monolayers are held together by van der Waals forces, which then combine to form the bulk material [13]. The three major polytypes of bulk MoS_2

* Corresponding author.
E-mail address: r.m.hartkamp@tudelft.nl (R. Hartkamp).

https://doi.org/10.1016/j.apsusc.2025.164284
Received 28 April 2025; Received in revised form 6 August 2025; Accepted 6 August 2025
Available online 18 August 2025

are the metastable 1T-polytype with octahedral structure and exhibiting metallic properties, the 3R- and the 2H-polytypes with trigonal prismatic structure (see Figure S1) and displaying semiconducting properties [14]. The 2H-polytype MoS_2 is composed of a two-layer stacked unit cell that restores the otherwise broken inversion symmetry of the monolayer MoS_2, while the 3R-polytype consists of a three-layer unit cell, where the inversion symmetry is broken [15,16].

Due to the broken inversion symmetry in the 3R-polytype, a strong spin–orbit coupling is possible based on the d-orbitals of the transition metals [17]. This provides the opportunity for the development of such applications as electronic and optoelectronic devices [18,19] and using properties such as valley- and spin-Hall effect and superconductivity [20–22]. The 3R-polytype can be synthesized through chemical vapor deposition and via the mechanical folding and stacking of MoS_2 monolayers [23,24]. Conversely, the 2H-polytype is the most commonly and naturally available polytype [14]. The applications with this polytype include utilizing bulk or monolayer MoS_2 as (electro-/photo-)catalyst both for hydrogen production in aqueous media [25–27] and for CO_2 reduction in organic media [28–30]. Furthermore, the 2H-polytype MoS_2 has demonstrated to be a suitable anode material for aqueous rechargeable batteries (ARBs) based on alkali earth metals [31–36], earth metals [37–40], and earth-abundant materials [41–43], as emerging competitors to lithium-ion batteries (LIBs).

As both the 2H and the 3R polytypes are semiconducting, the presence of the bandgap presents a challenge, but also an opportunity for tuning the electronic properties. The layered structure of MoS_2 allows the intercalation of (alkali metal) ions, which then donate their valence electrons to the MoS_2 and increase its conductivity and change the bandgap. If the intercalation occurs at high concentrations of intercalants, then a phase transition is induced from the 2H polytype phase to the metastable 1T-polytype phase by the gliding of the monolayers [44]. The intercalation process of different alkali metal ions was studied through various experimental techniques [45,46]. Wang et al. imaged the intercalation process of Na^+ ions in MoS_2 with aberration-corrected transmission electron microscopy (TEM) and they showed that the MoS_2 structure undergoes complicated phase transitions due to the presence of the Na^+ ions [45]. Attanayake et al. compared the intercalation of Na^+, Ca^{2+}, Co^{2+} and Ni^{2+} ions to MoS_2 based on the efficiency of hydrogen production [47]. The intercalation of K atoms and K^+ ions was studied by Andersen et al. using first-principle calculations [48]. Their calculations showed that the ions together with water molecules can be intercalated into the bulk MoS_2 structure; however, based on measurements by Zak et al. [49] they only added one or two water molecules next to the ions, not a full hydration shell.

Controlling intercalation on the microscale can significantly impact the property changes of the 2D material. However, achieving such control requires a mechanistic understanding of intercalation and the factors that influence it, such as the role of the intercalant and the material and its electronic properties. While the effects of different intercalants have been studied in the literature, a holistic and systematic comparison that links the mechanisms at the atomistic level to changes in material properties at the macroscopic level is still lacking.

The electrochemical intercalation process, where the driving force of the intercalation can be controlled externally, presents a path for this systematic comparison. Hence, this article aims to bridge this gap by shedding new light on the intercalation mechanism influenced by external and internal parameters, such as the applied voltage and the inherent hydration shell of the alkali metal ions. We use molecular dynamics (MD) simulations to show the microscopic mechanisms of the intercalation, while the macroscopic mechanisms and changes in the material properties are studied experimentally.

2. Methods and materials

2.1. Molecular dynamics simulations

All MD simulations were carried out in the Large-scale Atomic/Molecular Massively Parallel Simulator (LAMMPS) simulation package [50] using the DelftBlue supercomputer. For the MoS_2, the REBOMOS potential was used, developed by Jiang et al. [51]; the SPC/E water model was employed to describe the interactions between hydrogen and oxygen atoms in water molecules. The rigid structure of the water molecules was maintained using the SHAKE algorithm. A transferable ion force field, developed by Loche and co-workers [52], was used for KCl and NaCl. Packmol software was used to construct the simulation box. A detailed description of the MD simulations is provided in the Supplementary Information.

2.2. Electrode preparation

MoS_2 nanopowder (99% trace metal basis, Sigma Aldrich, for characterization see figures S7–S11) was mixed with Carbon Black (CB, Fischer Scientific) and poly(vinyl alcohol) (PVA) was mixed in a ratio of 90 wt%, 5 wt% and 5 wt%, respectively. Once the ingredients are measured and added to a 5 cm^3 vial, the mixture is diluted with 2 mL of Deionized (DI) water, then the ink is sonicated in a water bath for 10 min for homogenization. The glassy carbon substrates (1 × 1 cm, Sigma Aldrich, redox.me) are cleaned with DI water and then sonicated in isopropyl alcohol for 5 min, then dried with compressed air. After the sonication of the ink, 25 μL is dropcasted on the glassy carbon substrates; afterwards, the samples are left to dry in air. Afterwards, the electrodes are prepared by connecting a copper tape to the substrate and then it is covered with tape, exposing only a circle of 10 mm in diameter. Then, the intercalation of the two different alkali metal ions (Na^+ and K^+) in the MoS_2 was carried out to enhance its conductivity.

The intercalation of alkali metal ions into MoS_2 is known to induce a phase transition from the semiconducting 2H-phase to the metallic 1T-phase, which is metastable and prone to reversion to the 2H-phase upon thermal treatment or over time [53,54]. In particular, Li^+ and Na^+ ions can intercalate reversibly and stabilize the 1T-phase to some extent due to their smaller size, while K^+ ions, having a larger atomic radius, cause more pronounced lattice distortion and reduced reversibility [54]. The 1T-phase has been reported to transform back to the thermodynamically stable 2H-phase at temperatures as low as 95 °C [55]. To mitigate such phase relaxation, all sample processing and characterization steps were performed at room temperature or below.

2.3. Electrochemical techniques

All electrochemical measurements were carried out on a BioLogic VMP-3e Multichannel Potentiostat with the software EC-Lab. For each measurement the prepared electrode was immersed in 40 mL of 1 mM $KHCO_3$ (Sigma Aldrich, 99.99%) (K^+-intercalation) or 1 mM $NaHCO_3$ (Sigma Aldrich, 99.99%) (Na^+-intercalation) in an electrochemical H-cell. The electrode was placed in the cathode compartment together with a saturated calomel electrode (SCE), while a Pt mesh electrode was put in the anode compartment. All electrodes were then connected to the potentiostat and the whole system was put into a Faradaic cage. For the electrochemical intercalation, an electrochemical impedance spectroscopy (EIS) was first carried out from 1.0 MHz to 100 mHz, then a chronoamperometry (CA) measurement was set on for 1 h at a preset potential (the effect of potential was studied and an intercalation potential was defined for each ion). Afterwards, the working electrode was rinsed with DI water to remove any potential adsorbed layer and another EIS measurement was carried out to assess the conductivity of the sample.

2.4. Scanning electron microscopy

Scanning Electron Microscopy was performed using a JEOL IT800SHL system equipped with a field emission gun, operating at 10.00 kV and a beam current of 42.20 nA. Energy Dispersive Spectroscopy (EDS) analysis was conducted with an Oxford Instruments Maxim 100 detector.

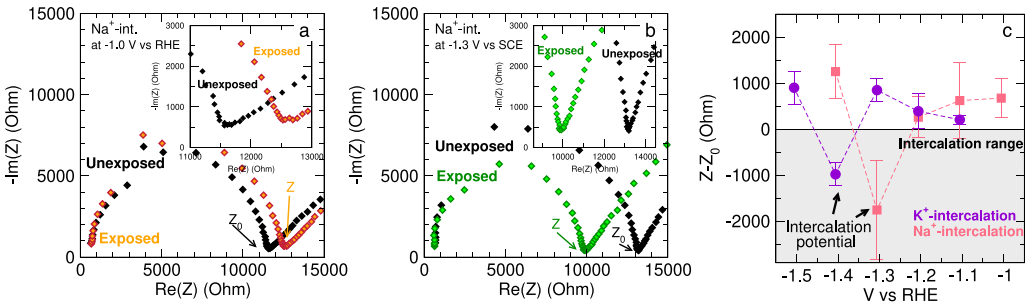

Fig. 1. Nquist plots for (a) unfavorable (−1.0 V vs RHE) and (b) favorable (−1.3 V vs RHE) conditions of electrochemical intercalation of sodium ions, (c) resistance change at different potentials due to (un)favorable conditions for the electrochemical intercalation of Na^+ and K^+ ions.

2.5. XRD

The XRD patterns were measured in a Bruker D8 Advance diffractometer with Bragg–Brentano geometry and Lynxeye position sensitive detector with Cu Kα radiation, divergence slit V12, scatter screen height 5 mm, at 45 kV and at 40 mA. The Detector was set to LL 0.11 W 0.14. The measurement range was set between 5° to 80°, with a step size of 0.03° (in case of the V_S-MoS_2 and K^+-intercalated V_S-MoS_2) and 0.06° (in case of the Na^+-intercalated V_S-MoS_2) with a counting time per step of 2 s.

2.6. Raman spectroscopy

The Raman spectra were obtained using a WiTec Alpha300R Raman Imaging microscope with a 532 nm laser at 1 mW power to prevent sample damage. The integration time was set to 5 s with 10 accumulations, and a 63X/0.9 water-dipping objective was used. To ensure high spectral resolution, a 1800 g/mm grating was employed, providing a resolution better than 1 cm^{-1}.

To accurately monitor structural changes induced by intercalation, in situ Raman measurements were performed at the exact same position on the sample surface before and after the electrochemical process. The sample was mounted in a beaker filled with the electrolyte, which was fixed directly on the Raman stage. The initial (pristine) Raman spectrum was acquired while the sample was immersed in the electrolyte. Following this, the objective was retracted in the Z direction to remove it from the solution, and the electrochemical intercalation process was carried out. After intercalation, the objective was carefully repositioned to the same coordinates (The spatial positioning resolution of the system was approximately 25 nm in XYZ directions, enabling precise repositioning of the measurement spot) and focus depth to acquire the post-intercalation Raman spectrum. This ensured that the layer number and measurement location remained constant, and that any observed spectral changes originated from structural modifications, such as defect formation, rather than sample drift, delamination, or layer number variation.

2.7. X-ray photoelectron spectroscopy

X-ray photoelectron spectroscopy was carried out in a Physical Electronics (PHI) 5400 (Eden Prairie, USA) instrument. The XPS spectra were acquired by using non-monochromatic Al Kα radiation produced from an X-ray source with an Al anode, operating at 200 W and 13.5 kV. The primary photoelectron lines for each element were captured with a step size of 0.1 eV and a dwell time of 1.25 s, employing a spherical capacitor analyzer configured with a pass energy of 71.55 eV. The MultiPak software was used to analyze and process the XPS data, where the acquired peaks were normalized and fitted using the iterated-Shirley background.

3. Results and discussions

3.1. Electrochemical intercalation

The insertion of Na^+- and K^+-ions into MoS_2 was achieved via electrochemical intercalation by applying a constant potential on the working electrode. Electrochemical impedance spectroscopy (EIS) measurements before and after the intercalation steps are used as an indicator of changes in conductivity, suggesting favorable conditions for intercalation. Figs. 1(a) and (b) show the Nyquist plots of unfavorable and favorable conditions, respectively, where Z_0 is the charge transfer resistance belonging to the unexposed electrode and Z is the charge transfer resistance belonging to the electrode which was subjected to chronoamperometry for 1 h at the respective potentials. The position of Z with respect to Z_0 determines if the potential of the chronoamperometry can be considered as a favorable or unfavorable condition for electrochemical intercalation. In Fig. 1(a), a case of unfavorable condition is presented, where it shows that the internal resistance (the sum of the electrolyte resistance and the charge transfer resistance [56]) of the intercalated electrode is higher than the unexposed electrode, namely $Z > Z_0$. On the other hand, Fig. 1(b) shows the favorable conditions for intercalation, where the internal resistance of the exposed electrode is smaller than that of the unexposed electrode, namely $Z < Z_0$. This relation indicates favorable conditions for intercalation, which results in a lower charge transfer resistance and, therefore, a higher conductivity. The data from different measurements at different potentials are collected in Tables S1 and S2 for sodium and potassium intercalation, respectively.

Fig. 1(c) shows the averaged difference of the measured resistance of the electrode at different applied potentials. A negative difference indicates a drop in the internal resistance of the electrode due to intercalation. Where the Z-Z_0 value is strongly negative, they were labeled as 'intercalation potential' for each ion, namely for potassium −1.4 V vs RHE, for sodium −1.3 V vs RHE, respectively.

3.2. MD simulations

MD simulations with umbrella sampling were used to study the intercalation mechanism of the Na^+ and K^+ ions. A simulation box (19.3 nm × 9.4 nm × 4.4 nm) was created with 18 000 water molecules, 4 MoS_2 sheets, containing 2700 atoms per sheet, and one cation (Na^+ or K^+) with one Cl^- ion for charge neutrality. A description of simulation details and the cross-interaction parameter optimization to reproduce the correct wettability can be found in the Supplementary Information (Tables S3 and S4, Figures S2-S5).

The intercalation Gibbs free-energy curves are shown in Fig. 2(a). The hydration shell of Na^+ and K^+ in bulk water contains approximately 6 and 7 water molecules on average, respectively [57,58]. Intercalation of these ions into MoS_2 requires the hydration shell to be perturbed, resulting in an energy barrier at the edge of the MoS_2. This energy barrier for intercalation is almost twice as high for the K^+

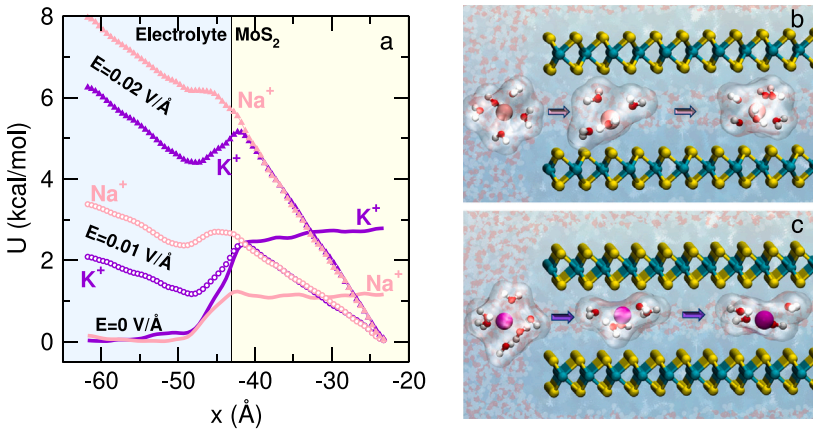

Fig. 2. (a) Gibbs free-energy curves for non-biased (E=0 V/Å) and biased (E=-0.01 V/Å and E=-0.02 V/Å) intercalation. (b and c) Merged snapshots from MD simulations of Na^+-intercalation and K^+-intercalation, respectively, showing the deformation of the hydration shells of the ions upon intercalation (molybdenum atoms are represented with blue color, sulfur atoms are represented with yellow color, sodium ions are represented with pink color, potassium ions are represented with purple color).

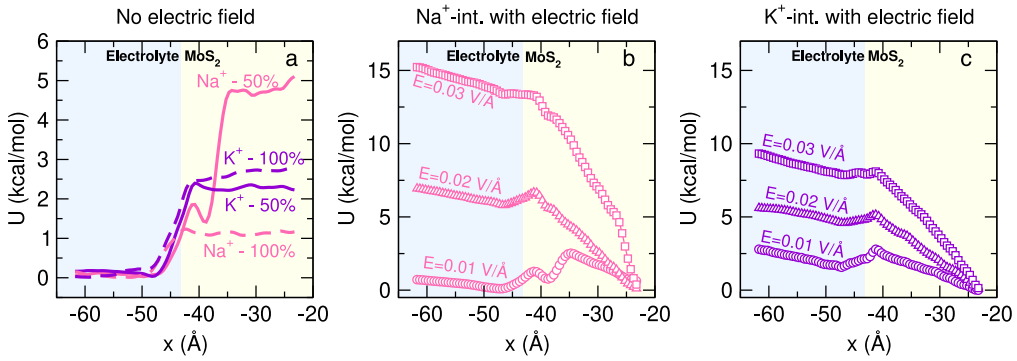

Fig. 3. (a) Gibbs free-energy profiles when no electric field is present, (b) and (c) Gibbs free-energy profiles of sodium and potassium ions in a geometry of 50% hydrated MoS_2 and different electric fields are present.

ion as for the Na^+ ion, despite the larger hydration energy of the latter ion [59].

If an external electric field is applied to the system, in accordance with our experiments, then a force $F = qE$ acts on each charged atom, where q is the charge and E is the electric field. The external electric field acts as an additional driving force for the ion insertion in the interlayers of the MoS_2. By applying 0.01 V/Å, the intercalation barrier for Na^+ and K^+ ions is lowered by about half relative to the case without an external field applied. However, the barrier remains larger than the thermal energy $E_{th} = RT \approx 0.59$ kcal/mol, such that intercalation events are not likely to occur on the simulation time scale. At 0.02 V/Å, the intercalation barrier has vanished for Na^+, whereas a barrier remains for K^+.

Figs. 2(b and c) present merged snapshots of the MD simulations showing the difference between the disruption of the hydration shells of the two ions. The hydration shell of the Na^+ ion is only perturbed and deformed during the intercalation process, whereas the K^+ ion has to expel at least one water molecule from its shell to fit in the interlayer distance. Furthermore, the remaining shell is still sterically disrupted, hence the higher energy barrier for intercalation. This confirms the trend of the different energy barriers in the Gibbs free-energy profiles in Fig. 2(a), which then connects and explains well the higher experimental intercalation energy for potassium in Fig. 1(c).

These results deviate from the results of Andersen et al. [48], where only two water molecules were included in the hydration shell. Their computations were based on the work by Zak et al. [49] who measured a 50% increase in the vertical lattice parameter and suggested that one or two water molecules per K atom are also intercalated in the MoS_2. To test if their assumption is accurate, we also decreased the hydration of the MoS_2 to 50%, mimicking the 50% vertical lattice parameter increase. The simulation snapshots in Figure S6 (a) and (c) show the perturbation of the hydration shell upon interaction of the ion. The hydration shell of the ions is more deformed than those in the case of a fully hydrated MoS_2. The hydration shell around both ions adopts a planar configuration containing four water molecules, which exceeds the two water molecules reported by Zak et al. [49]. The Gibbs free-energy curves for these 50% MoS_2 hydration cases in the absence of an externally applied electric field are shown in Fig. 3(a). Here, a switch in energy barrier trend can be observed: as the sodium ion has a stronger hydration shell, it presents a larger energy barrier for intercalation compared to the intercalation energy barrier of the potassium ion which stays almost the same as for 100% MoS_2 hydration. Figs. 3(b) and (c) show that the intercalation energy barrier of both ions drastically decreases if an external electric field is applied. The difference between the experimental and computational models stems from practical limitations in atomistic simulations, where a small, idealized system is used to represent a local region of the larger experimental structure, allowing key intercalation trends to be captured within feasible computational resources.

3.3. Structure analysis

Structural and surface characterization methods are used to study the effect of the electrochemical intercalation on the structural properties of MoS_2. Fig. 4(a) shows the XRD patterns of the intercalated and non-intercalated MoS_2. The intensity of the main peak at the (002) crystal plane orientation for the Na^+-intercalated and K^+-intercalated electrodes weakens with respect to the non-intercalated MoS_2 and a

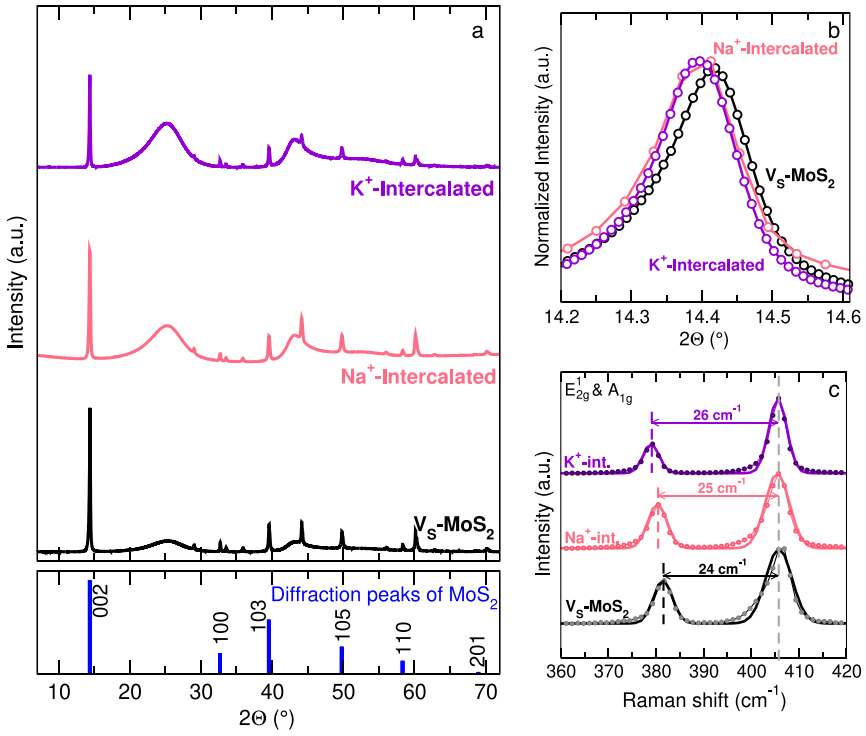

Fig. 4. (a) XRD pattern of V_S-MoS_2, Na^+-intercalated V_S-MoS_2 and K^+-intercalated V_S-MoS_2. (b) XRD pattern showing a slight shift in (002) crystal plane orientation of Na^+-intercalated V_S-MoS_2 and K^+-intercalated V_S-MoS_2 with respect to V_S-MoS_2. (c) Raman spectra focused on E^1_{2g} and A_{1g} modes. (All spectra were normalized to their respective A_{1g} peak and the plots were stacked for maximum visibility of the shift).

slight broadening can also be observed (Fig. 4(b)), which indicates a decrease of the crystallinity as a consequence of the intercalation [45]. Furthermore, this can also indicate irreversible changes in the crystal structure [45]. This slight broadening can better be observed in Fig. 4(b), which also shows a slight shift of the peak at the (002) crystal plane orientation to smaller angles, which corresponds to an interlayer expansion due to the intercalation [60].

Raman spectroscopy (Fig. 4(c)) was carried out to confirm the presence of vacancies indicated by XRD. Bulk MoS_2 has four characteristic modes in the Raman spectrum E^2_{2g}, E_{1g}, E^1_{2g} and A_{1g}, at ~32 cm^{-1} at ~286 cm^{-1}, at ~384.5 cm^{-1} and at ~405.5 cm^{-1}, respectively [61]. Figure S8 shows all the mentioned characteristic modes except E^2_{2g} due to the limitation of low-frequency measurements of the instrument. The peaks appearing between ~430 cm^{-1} and ~470 cm^{-1} are due to the near-the-zone-edge longitudinal and acoustic phonons and their combinations [62]. The two main peaks, E^1_{2g} and A_{1g}, are characteristic of different vibrations of the material: E^1_{2g} is activated by the in-plane vibrations of the Mo and S atoms, while A_{1g} is activated by out-of-plane vibrations of the S atoms [61,63].

Fig. 4(c) shows the E^1_{2g} and A_{1g} modes stacked for intercalated and non-intercalated electrodes. The A_{1g} mode was measured at 405.7 cm^{-1} for all samples, while for the intercalated samples, the E^1_{2g} shows a shift to lower frequencies compared to the non-intercalated electrode. The increased separation between the E^1_{2g} and A_{1g} modes indicates a compressive strain in the MoS_2 structure due to the presence of monosulfur defects [64]. The creation of these monosulfur defects is a consequence of the unused electrode preparation process, hence, this difference in the spectra can also be used for the estimation of the defect concentration in MoS_2 [65,66]. For a structurally pristine MoS_2, the difference between the E^1_{2g} and A_{1g} peaks is 21 cm^{-1} [61], whereas this value has already increased to 24 cm^{-1} for our MoS_2 electrode. This suggests that monosulfur defects are created in the electrode (from now denoted as V_S-MoS_2) during the sonication step of the sample preparation process. The further blue-shift of the E^1_{2g} peaks of the intercalated samples compared to the V_S-MoS_2 electrode indicates an increased concentration of monosulfur vacancies as a consequence of the intercalation process and confirms our findings in the XRD patterns [64,67].

3.4. XPS analysis

Fig. 5(a) shows the Mo 3d XPS spectra of V_S-MoS_2, Na^+-intercalated and K^+-intercalated V_S-MoS_2. The monosulfur vacancies in the MoS_2 structure identified with Raman spectroscopy are also confirmed with the presence of undercoordinated Mo sites (Mo^{UC}) in the Mo 3d spectra [68,69]. In these fitted Mo 3d spectra, the area (Table S6) of the Mo^{UC} atoms is increased for the intercalated V_S-MoS_2 compared to the V_S-MoS_2. This also correlates with the results from the Raman spectroscopy, as the concentration of these undercoordinated Mo sites in the XPS spectra increases with the same tendency as the concentration of the monosulfur defects increases in the Raman spectra. In all three fits, a small peak at a ~234.5 eV and ~235.5 eV can be observed, which corresponds to the oxidation state of Mo^{6+} in MoO_3, which can be present due to the exposure to air and water in the ink during the sample preparation process and in the electrolyte during the electrochemical intercalation [46,70].

For V_S-MoS_2, the two main peaks, Mo $3d_{5/2}$ and $3d_{3/2}$for the V_S-MoS_2 are located at 229.1 eV and 232.4 eV, respectively, which agree with the literature values [45,71]. Fig. 5(a) also shows the shift in the binding energy for the intercalated V_S-MoS_2 electrodes with respect to the V_S-MoS_2 electrode. However, these peaks are down-shifted for the Na^+-intercalated and K^+-intercalated V_S-MoS_2 by 0.5 eV and 0.7 eV, respectively, which indicates the presence of excess electrons compared to the V_S-MoS_2. This also suggests that electrons were donated from the intercalants (Na^+ and K^+ ions) to the V_S-MoS_2 [45]. The same downshift in energy was observed for the S 2p3 spectra of the three materials (see Figure S10 (a)).

The degree of alkali metal intercalation into V_S-MoS_2 was estimated based on the observed binding energy shifts in the XPS spectra. Specifically, shifts of 0.6 eV for K^+ and 0.5 eV for Na^+ in the Mo 3d core level

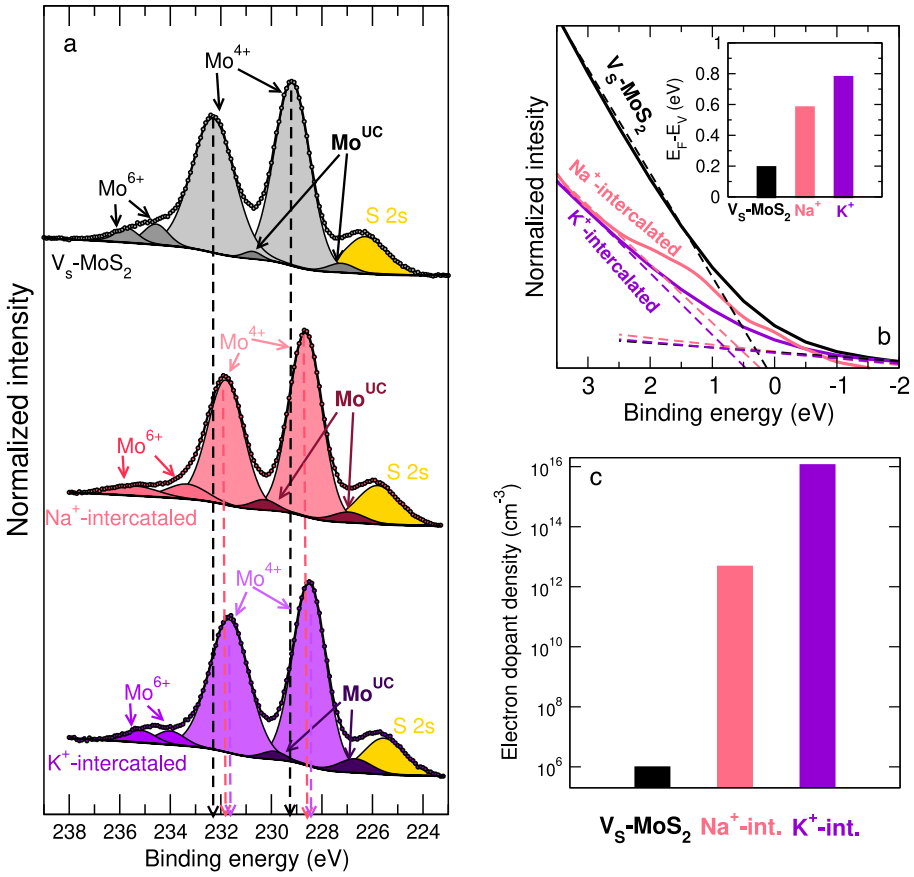

Fig. 5. (a) Fitting of normalized Mo 3d XPS spectra of V_S-MoS_2, Na^+-intercalated V_S-MoS_2 and K^+-intercalated V_S-MoS_2, respectively, the spectra of the intercalated V_S-MoS_2 compared to V_S-MoS_2 spectrum showing a down-shift in binding energy. (b) Linear fitting of valence band spectra to determine E_F-E_V (shown in inset). (c) Calculated electron doping density of pristine, Na^+-intercalated and K^+-intercalated V_S-MoS_2 based on valence band spectra showing the amount of electron dopants for each electrode.

suggest a significant level of intercalation. Comparing our results to literature benchmarks, these chemical shifts correspond to intercalation levels of approximately $x \approx 0.3$–0.5 in A_xMoS_2 [72–74]. These levels are known to induce measurable structural and electronic changes, supporting the observed modifications in our system.

To study the effect of the intercalation on the electronic structure of the V_S-MoS_2 further, Figs. 5(b) and (c) assess the effect of intercalation on the valence band, hence, high-resolution XPS measurements were taken from 20 eV to −15 eV. The value of the bandgap can be changed through intercalation of alkali metal ions and, consequently, electron doping [48]. The intercalation of the alkali metal ions changes the slope of the spectra and, hence, changes the energy level difference between the Fermi level and the valence band (E_F-E_V). With a linear extrapolation to the valence band tail (near 0 eV binding energy) in the XPS spectra, the value of E_F-E_V was determined, where E_F is the Fermi level energy and E_V is the valence band energy, respectively [75].

The high electron dopant density for the Na^+-intercalated and K^+-intercalated V_S-MoS_2 is a consequence of the synergy between the sulfur defects and donated s-electrons of the alkali metal ions. The change in the electronic properties of lithiated and sodiated defective MoS_2 has already been investigated with density functional theory (DFT) by Barik et al. [76]. According to the DFT calculations, the sulfur defects create a midgap state and reduce the bandgap significantly. The adsorption of the intercalants (lithium and sodium in their case) is enhanced as the midgap state coming from the d-orbital of the Mo atom and the s-orbital of the alkali metal atom forms a strong hybridization. This results in an enhanced conductivity and changes the semiconducting nature of the defective MoS_2 to metallic with the lithiation/sodiation. Our experimental results correlate well with these calculations in the case of the Na^+-intercalated V_S-MoS_2. However, for the K^+-intercalated V_S-MoS_2 the electron dopant density is even higher, which can be due to the presence of potassium's empty *d*-orbital. The separation of light (Li^+ and Na^+) and heavy alkali metal ions (K^+, Rb^+ and Cs^+) are based on the presence of this empty *d*-orbital, as it gives the possibility of further hybridization between the heavy alkali metal's *d*-orbital and the transition metal's *p*-orbital. This hybridization and the charge transfer then create a low work function due to a larger dipole moment than for light alkali metals [77]. This behavior is similar to what Yu et al. found with regards to the intercalation of sodium and potassium ions in Cu_4Se_4 [78,79]. Intercalation of alkali-metal ions into Cu_4Se_4 nanosheets induces a surface phase transition, with K^+ intercalation occurring at a higher voltage (0.756 V) than Na^+ (0.659 V), indicative of stronger charge transfer [78]. This stronger interaction leads to a larger surface dipole and therefore a more pronounced decrease in work function for K^+-intercalated Cu_4Se_4 compared to the Na^+-intercalated counterpart [78].

4. Conclusions

In this work, we have studied the intercalation mechanisms of Na^+ and K^+ ions into MoS_2 and their effect on the structural and electronic properties of the host material. We have found that the intercalation energy strongly depends on the perturbed hydration shell of the alkali metal ion in an aqueous environment at the interface with the MoS_2. Furthermore, we have shown that the intercalation process increases the concentration of monosulfur defects in the MoS_2 structure. However, the presence of these defects and the donated electrons from the alkali metal ions have a synergistic effect on the electronic material properties, resulting in increased conductivity. The difference between the level of electron dopant density with regard to light and heavy

alkali metal ions can be attributed to the presence of the empty orbitals, which allow further hybridization. These results also have shown that MoS_2 is a highly tunable material regarding not only its structural properties, regarding its flexibility in the vertical dimension, but also its electronic properties through changing the valance band structure; and that the structure engineered on the atomic scale has a large influence on the macroscopic properties.

CRediT authorship contribution statement

Eszter Mádai: Writing – original draft, Visualization, Methodology, Investigation, Conceptualization. **Prasaanth Ravi Anusuyadevi:** Writing – review & editing, Investigation, Conceptualization. **Prasad Gonugunta:** Writing – review & editing, Investigation. **Amirhossein Mohseni Armaki:** Writing – original draft, Investigation. **Arjan Mol:** Writing – review & editing, Supervision. **Peyman Taheri:** Writing – review & editing, Supervision, Resources. **Remco Hartkamp:** Writing – review & editing, Visualization, Supervision, Investigation, Formal analysis.

Declaration of competing interest

The authors declare that they have no known competing financial interests or personal relationships that could have appeared to influence the work reported in this paper.

Appendix A. Supplementary data

Supplementary material related to this article can be found online at https://doi.org/10.1016/j.apsusc.2025.164284.

Data availability

Data will be made available on request.

References

[1] M. Akhtar, G. Anderson, R. Zhao, A. Alruqi, J.E. Mroczkowska, G. Sumanasekera, J.B. Jasinski, Recent advances in synthesis, properties, and applications of phosphorene, Npj 2D Mater. Appl. 1 (1) (2017) 5, http://dx.doi.org/10.1038/s41699-017-0007-5.

[2] P.R. Anusuyadevi, S. Pranavi, R.N.R. Shaw, E. Mádai, D.J.P. Kumar, P. Gonugunta, P. Taheri, A. Mol, An overview of emerging 2D nanomaterials: General synthesis methods and properties, in: Next-generation 2D nanomaterials for sustainable energy and environment-oriented applications: Electrocatalysis, photoelectrocatalysis and photocatalysis, R. Soc. Chem. (2025) http://dx.doi.org/10.1039/9781837675838-00001.

[3] L. Zhang, K. Liu, Z. Chen, Y. Wang, Advances in 2D materials for catalytic applications: A review, J. Colloid Interface Sci. 695 (2025) 137799, http://dx.doi.org/10.1016/j.jcis.2023.137799.

[4] Y.-X. Yu, Oxygen-transfer from N_2O to co via y-doped Ti_2Co_2 (MXene) monolayer at room temperature: Density functional theory and ab initio molecular simulation studies, J. Colloid Interface Sci. (2025) 137799.

[5] B. Radisavljevic, A. Radenovic, J. Brivio, V. Giacometti, A. Kis, Single-layer MoS_2 transistors, Nature Nanotechnology 6 (3) (2011) 147–150, http://dx.doi.org/10.1038/nnano.2010.279.

[6] H. Liu, L. Zhao, T. Zhang, J. Li, Recent progress of 2D materials in energy storage and conversion, Appl. Surf. Sci. 546 (2021) 149062, http://dx.doi.org/10.1016/j.apsusc.2021.149062.

[7] Y. Xin, Y.-X. Yu, Possibility of bare and functionalized niobium carbide MXenes for electrode materials of supercapacitors and field emitters, Mater. Des. 130 (2017) 512–520.

[8] J.Z. Hassan, A. Raza, Z.U. Din Babar, U. Qumar, N.T. Kaner, A. Cassinese, 2D material-based sensing devices: an update, J. Mater. Chem. A 11 (12) (2023) 6016–6063, http://dx.doi.org/10.1039/d2ta07653e.

[9] F. Zhang, C. Li, Z. Li, L. Dong, J. Zhao, Recent progress in three-terminal artificial synapses based on 2D materials: from mechanisms to applications, Microsystems & Nanoeng. 9 (1) (2023) 16, http://dx.doi.org/10.1038/s41378-023-00487-2.

[10] Y.-C. Lin, R. Torsi, R. Younas, C.L. Hinkle, A.F. Rigosi, H.M. Hill, K. Zhang, S. Huang, C.E. Shuck, C. Chen, Y.-H. Lin, D. Maldonado-Lopez, J.L. Mendoza-Cortes, J. Ferrier, S. Kar, N. Nayir, S. Rajabpour, A.C.T. van Duin, X. Liu, D. Jariwala, J. Jiang, J. Shi, W. Mortelmans, R. Jaramillo, J.M.J. Lopes, R. Engel-Herbert, A. Trofe, T. Ignatova, S.H. Lee, Z. Mao, L. Damian, Y. Wang, M.A. Steves, K.L.J. Knappenberger, Z. Wang, S. Law, G. Bepete, D. Zhou, J.-X. Lin, M.S. Scheurer, J. Li, P. Wang, G. Yu, S. Wu, D. Akinwande, J.M. Redwing, M. Terrones, J.A. Robinson, Recent advances in 2D material theory, synthesis, properties, and applications, ACS Nano 17 (11) (2023) 9694–9747, http://dx.doi.org/10.1021/acsnano.2c12759, pMID: 37219929.

[11] Z.-H. Wu, Y.-X. Yu, Theoretical study on catalytic performance of Ti_2B monolayer as cathodes of Li–O_2 and Na–O_2 batteries promoted by surface functionalization, Appl. Surf. Sci. 666 (2024) 160380, http://dx.doi.org/10.1016/j.apsusc.2024.160380.

[12] S. Joseph, J. Mohan, S. Lakshmy, S. Thomas, B. Chakraborty, S. Thomas, N. Kalarikkal, A.review.of.the. synthesis, properties, And applications of 2D transition metal dichalcogenides and their heterostructures, Mater. Chem. Phys. 297 (2023) 127332, http://dx.doi.org/10.1016/j.matchemphys.2023.127332.

[13] L.F. Mattheiss, Band structures of transition-metal-dichalcogenide layer compounds, Phys. Rev. B 8 (8) (1973) 3719–3740, http://dx.doi.org/10.1103/physrevb.8.3719.

[14] J. Wilson, A. Yoffe, The transition metal dichalcogenides discussion and interpretation of the observed optical, electrical and structural properties, Adv. Phys. 18 (73) (1969) 193–335, http://dx.doi.org/10.1080/00018736900101307.

[15] X. Fan, W. Zheng, J. Kuo, D.J. Singh, C. Sun, W. Zhu, Modulation of electronic properties from stacking orders and spin–orbit coupling for 3R-type MoS_2, Sci. Rep. 6 (24140) (2016) http://dx.doi.org/10.1038/srep24140.

[16] S. Thomas, S. Moolayadukkam, K.P. Priyanka, Structural, mechanical, and electronic properties of in-plane 1T/2H-MoS_2, 2H-MoS_2, and 3R-MoS_2, in: Structural, Mechanical, and Electronic Properties of in-Plane 1T/2H-MoS_2, 2H-MoS_2, and 3R-MoS_2, Springer Nature Singapore, Singapore, 2024.

[17] W. Feng, Y. Yao, W. Zhu, J. Zhou, W. Yao, D. Xiao, Intrinsic spin hall effect in monolayers of group-vi dichalcogenides: A first-principles study, Phys. Rev. B 86 (16) (2012) 165108, http://dx.doi.org/10.1103/PhysRevB.86.165108.

[18] Q.H. Wang, K. Kalantar-Zadeh, A. Kis, J.N. Coleman, M.S. Strano, Electronics and optoelectronics of two-dimensional transition metal dichalcogenides, Nature Nanotechnology 7 (11) (2012) 699–712, http://dx.doi.org/10.1038/nnano.2012.193.

[19] B. Radisavljevic, A. Radenovic, J. Brivio, V. Giacometti, A. Kis, Single-layer MoS_2 transistors, Nature Nanotechnology 6 (3) (2011) 147–150, http://dx.doi.org/10.1038/nnano.2010.279.

[20] Z.Y. Zhu, Y.C. Cheng, U. Schwingenschlögl, Giant spin–orbit-induced spin splitting in two-dimensional transition-metal dichalcogenide semiconductors, Phys. Rev. B 84 (15) (2011) 153402, http://dx.doi.org/10.1103/physrevb.84.153402.

[21] H. Zeng, J. Dai, W. Yao, D. Xiao, X. Cui, Valley polarization in MoS_2 monolayers by optical pumping, Nature Nanotechnology 7 (8) (2012) 490–493, http://dx.doi.org/10.1038/nnano.2012.95.

[22] R. Roldán, E. Cappelluti, F. Guinea, Interactions and superconductivity in heavily doped MoS_2, Phys. Rev. B 88 (2013) 054515, http://dx.doi.org/10.1103/PhysRevB.88.054515.

[23] R. Suzuki, M. Sakano, Y.J. Zhang, R. Akashi, D. Morikawa, A. Harasawa, K. Yaji, K. Kuroda, K. Miyamoto, T. Okuda, K. Ishizaka, R. Arita, Y. Iwasa, Valley-dependent spin polarization in bulk MoS_2 with broken inversion symmetry, Nature Nanotechnology 9 (8) (2014) 611–617, http://dx.doi.org/10.1038/nnano.2014.148.

[24] K. Liu, L. Zhang, T. Cao, C. Jin, D. Qiu, Q. Zhou, A. Zettl, P. Yang, S.G. Louie, F. Wang, Evolution of interlayer coupling in twisted molybdenum disulfide bilayers, Nat. Commun. 5 (1) (2014) 4966, http://dx.doi.org/10.1038/ncomms5966.

[25] H. Wang, X. Xiao, S. Liu, C.-L. Chiang, X. Kuai, C.-K. Peng, Y.-C. Lin, X. Meng, J. Zhao, J. Choi, Y.-G. Lin, J.-M. Lee, L. Gao, Structural and electronic optimization of MoS_2 edges for hydrogen evolution, J. Am. Chem. Soc. 141 (46) (2019) 18578–18584, http://dx.doi.org/10.1021/jacs.9b09932.

[26] Y. Shi, Y. Zhou, D.-R. Yang, W.-X. Xu, C. Wang, F.-B. Wang, J.-J. Xu, X.-H. Xia, H.-Y. Chen, Energy level engineering of MoS_2 by transition-metal doping for accelerating hydrogen evolution reaction, J. Am. Chem. Soc. 139 (43) (2017) 15479–15485, http://dx.doi.org/10.1021/jacs.7b08881.

[27] Y. Yu, S.-Y. Huang, Y. Li, S.N. Steinmann, W. Yang, L. Cao, Layer-dependent electrocatalysis of MoS_2 for hydrogen evolution, Nano Lett. 14 (2) (2014) 553–558, http://dx.doi.org/10.1021/nl403620g, pMID: 24397410.

[28] P. Abbasi, M. Asadi, C. Liu, S. Sharifi-Asl, B. Sayahpour, A. Behranginia, P. Zapol, R. Shahbazian-Yassar, L.A. Curtiss, A. Salehi-Khojin, Tailoring the edge structure of molybdenum disulfide toward electrocatalytic reduction of carbon dioxide, ACS Nano 11 (1) (2016) 453–460, http://dx.doi.org/10.1021/acsnano.6b06392.

[29] M. Asadi, B. Kumar, A. Behranginia, B.A. Rosen, A. Baskin, N. Repnin, D. Pisasale, P. Phillips, W. Zhu, R. Haasch, Robust carbon dioxide reduction on molybdenum disulphide edges, Nat. Commun. 5 (1) (2014) 4470.

[30] M. Asadi, K. Kim, C. Liu, A.V. Addepalli, P. Abbasi, P. Yasaei, P. Phillips, A. Behranginia, J.M. Cerrato, R. Haasch, P. Zapol, B. Kumar, R.F. Klie, J. Abiade, L.A. Curtiss, A. Salehi-Khojin, Nanostructured transition metal dichalcogenide electrocatalysts for CO_2 reduction in ionic liquid, Science 353 (6298) (2016) 467–470, http://dx.doi.org/10.1126/science.aaf4767.

[31] L. Chen, Z. Chen, L. Chen, P. Zhou, J. Wang, H. Yang, Z. Feng, X. Li, J. Huang, The exfoliation of bulk MoS_2 by a three-roller mill for high-performance potassium ion batteries, Appl. Surf. Sci. 615 (2023) 156253, http://dx.doi.org/10.1016/j.apsusc.2022.156253.

[32] J. Li, F. Hu, H. Wei, J. Hei, Y. Yin, G. Liu, N. Wang, H. Wei, Confining MoS_2/c nanoparticles on two-dimensional graphene sheets for high reversible capacity and long-life potassium ions batteries, Compos. Part B: Eng. 250 (2023) 110424, http://dx.doi.org/10.1016/j.compositesb.2022.110424.

[33] J. Zheng, F. Xiao, H. Jin, C. Cao, Z. Lei, Y. Wang, M. Wei, Q. Qian, L. Zeng, Q. Chen, Facile fabrication of MoS_2 nanocrystals confined in waste leather derived n, p co-doped carbon fiber for long-lifespan of sodium/potassium ion batteries, J. Phys. Chem. Solids 172 (2023) 111080, http://dx.doi.org/10.1016/j.jpcs.2022.111080.

[34] J. Huang, Y. Yao, M. Huang, Y. Zhang, Y. Xie, M. Li, L. Yang, X. Wei, Z. Li, Creating unidirectional fast ion diffusion channels in g/NiS_2-MoS_2 heterostructures for high-performance sodium-ion batteries, Small 18 (18) (2022) 2200782, http://dx.doi.org/10.1002/smll.202200782.

[35] E.V. Sukhanova, L.A. Bereznikova, A.M. Manakhov, H.S.A. Qahtani, Z.I. Popov, A novel membrane-like 2D a'-MoS_2 as anode for lithium- and sodium-ion batteries, Membranes 12 (11) (2022) 1156, http://dx.doi.org/10.3390/membranes12111156.

[36] H. Zhang, J. Song, J. Li, J. Feng, Y. Ma, L. Ma, H. Liu, Y. Qin, X. Zhao, F. Wang, Interlayer-expanded MoS_2 nanoflowers vertically aligned on MXene@dual-phased TiO_2 as high-performance anode for sodium-ion batteries, ACS Appl. Mater. AndInterfaces 14 (14) (2022) 16300–16309, http://dx.doi.org/10.1021/acsami.2c02080.

[37] X. Fan, M. Tebyetekerwa, Y. Wu, R.R. Gaddam, X.S. Zhao, Magnesium/lithium hybrid batteries based on SnS_2-MoS_2 with reversible conversion reactions, Energy Mater. Adv. (2022) 1–14, http://dx.doi.org/10.34133/2022/9846797.

[38] M. Shao, H. Sheng, L. Lin, H. Ma, Q. Wang, J. Yuan, X. Zhang, G. Chen, W. Li, Q. Su, E. Xie, J. Wang, Z. Zhang, W. Lan, High-performance biodegradable energy storage devices enabled by heterostructured MoO_3 – MoS_2 composites, Small 19 (10) (2022) 2205529, http://dx.doi.org/10.1002/smll.202205529.

[39] M. Wang, H. Ye, V. Vasudevan, N.V. Medhekar, Enhancing kinetic and electrochemical performance of layered MoS_2 cathodes with interlayer expansion for Mg-ion batteries, J. Power Sources 542 (2022) 231722, http://dx.doi.org/10.1016/j.jpowsour.2022.231722.

[40] J.B.D. Linganay, D.B. Putungan, Adsorption and diffusion properties of calcium ions at the van der waals interface of $NbSe_2$-graphene 2D heterostructure for multivalent battery applications: density functional theory calculations, Mater. Res. Express 9 (9) (2022) 095506, http://dx.doi.org/10.1088/2053-1591/ac92c8.

[41] H. Liang, Z. Cao, F. Ming, W. Zhang, D.H. Anjum, Y. Cui, L. Cavallo, H.N. Alshareef, Aqueous zinc-ion storage in MoS_2 by tuning the intercalation energy, Nano Lett. 19 (5) (2019) 3199–3206, http://dx.doi.org/10.1021/acs.nanolett.9b00697.

[42] J. Liu, P. Xu, J. Liang, H. Liu, W. Peng, Y. Li, F. Zhang, X. Fan, Boosting aqueous zinc-ion storage in MoS_2 via controllable phase, Chem. Eng. J. 389 (2020) 124405, http://dx.doi.org/10.1016/j.cej.2020.124405.

[43] Z. Yao, W. Zhang, X. Ren, Y. Yin, Y. Zhao, Z. Ren, Y. Sun, Q. Lei, J. Wang, L. Wang, T. Ji, P. Huai, W. Wen, X. Li, D. Zhu, R. Tai, A volume self-regulation MoS_2 superstructure cathode for stable and high mass-loaded Zn-ion storage, ACS Nano 16 (8) (2022) 12095–12106, http://dx.doi.org/10.1021/acsnano.2c02330.

[44] Z. Wang, Q. Tu, S. Zheng, J.J. Urban, S. Li, B. Mi, Understanding the aqueous stability and filtration capability of MoS_2 membranes, Nano Lett. 17 (12) (2017) 7289–7298, http://dx.doi.org/10.1021/acs.nanolett.7b02804.

[45] X. Wang, X. Shen, Z. Wang, R. Yu, L. Chen, Atomic-scale clarification of structural transition of MoS_2 upon sodium intercalation, ACS Nano 8 (11) (2014) 11394–11400, http://dx.doi.org/10.1021/nn505501v.

[46] G. Wang, Y. Zhang, H.S. Cho, X. Zhao, F. Kim, J. Zou, Revisiting the structural evolution of MoS_2 during alkali metal (Li, Na, and K) intercalation, ACS Appl. Energy Mater. 4 (12) (2021) 14180–14190, http://dx.doi.org/10.1021/acsaem.1c02937.

[47] N.H. Attanayake, A.C. Thenuwara, A. Patra, Y.V. Aulin, T.M. Tran, H. Chakraborty, E. Borguet, M.L. Klein, J.P. Perdew, D.R. Strongin, Effect of intercalated metals on the electrocatalytic activity of 1T-MoS_2 for the hydrogen evolution reaction, ACS Energy Lett. 3 (1) (2017) 7–13, http://dx.doi.org/10.1021/acsenergylett.7b00865.

[48] A. Andersen, S.M. Kathmann, M.A. Lilga, K.O. Albrecht, R.T. Hallen, D. Mei, First-principles characterization of potassium intercalation in hexagonal 2H-MoS_2, J. Phys. Chem. C 116 (2) (2012) 1826–1832, http://dx.doi.org/10.1021/jp206555b.

[49] A. Zak, Y. Feldman, V. Lyakhovitskaya, G. Leitus, R. Popovitz-Biro, E. Wachtel, H. Cohen, S. Reich, R. Tenne, Alkali metal intercalated fullerene-like MS_2 (M=W, Mo) nanoparticles and their properties, J. Am. Chem. Soc. 124 (17) (2002) 4747–4758, http://dx.doi.org/10.1021/ja012060q.

[50] A.P. Thompson, H.M. Aktulga, R. Berger, D.S. Bolintineanu, W.M. Brown, P.S. Crozier, P.J. in 't Veld, A. Kohlmeyer, S.G. Moore, T.D. Nguyen, R. Shan, M.J. Stevens, J. Tranchida, C. Trott, S.J. Plimpton, LAMMPS - a flexible simulation tool for particle-based materials modeling at the atomic, meso, and continuum scales, Comput. Phys. Comm. 271 (2022) 108171, http://dx.doi.org/10.1016/j.cpc.2021.108171.

[51] J.-W. Jiang, H.S. Park, T. Rabczuk, Molecular dynamics simulations of single-layer molybdenum disulphide (MoS_2): Stillinger-weber parametrization, mechanical properties, and thermal conductivity, J. Appl. Phys. 114 (6) (2013) 064307, http://dx.doi.org/10.1063/1.4818414.

[52] P. Loche, P. Steinbrunner, S. Friedowitz, R.R. Netz, D.J. Bonthuis, Transferable ion force fields in water from a simultaneous optimization of ion solvation and ion–ion interaction, J. Phys. Chem. B 125 (30) (2021) 8581–8587, http://dx.doi.org/10.1021/acs.jpcb.1c05303.

[53] K.E. Dungey, M.D. Curtis, J.E. Penner-Hahn, Structural characterization and thermal stability of MoS_2 intercalation compounds, Chem. Mater. 10 (8) (1998) 2152–2161, http://dx.doi.org/10.1021/cm9800341.

[54] J. Zhang, A. Yang, X. Wu, et al., Reversible and selective ion intercalation through the top surface of few-layer MoS_2, Nat. Commun. 9 (2018) 5289, http://dx.doi.org/10.1038/s41467-018-07710-z.

[55] A.N. Enyashin, G. Seifert, New route for stabilization of 1T-WS_2 and MoS_2 phases, J. Phys. Chem. C 115 (50) (2011) 24586–24591, http://dx.doi.org/10.1021/jp2076325.

[56] B.-A. Mei, O. Munteshari, J. Lau, B. Dunn, L. Pilon, Physical interpretations of nyquist plots for edlc electrodes and devices, J. Phys. Chem. C 122 (1) (2017) 194–206, http://dx.doi.org/10.1021/acs.jpcc.7b10582.

[57] R. Hartkamp, B. Coasne, Structure and transport of aqueous electrolytes: From simple halides to radionuclide ions, J. Chem. Phys. 141 (12) (2014) 124508, http://dx.doi.org/10.1063/1.4896380.

[58] J. Mähler, I. Persson, A study of the hydration of the alkali metal ions in aqueous solution, Inorg. Chem. 51 (1) (2011) 425–438, http://dx.doi.org/10.1021/ic2018693.

[59] M.F. Döpke, O.A. Moultos, R. Hartkamp, On the transferability of ion parameters to the tip4p/2005 water model using molecular dynamics simulations, J. Chem. Phys. 152 (2) (2020) 024501, http://dx.doi.org/10.1063/1.5124448.

[60] K.D. Rasamani, F. Alimohammadi, Y. Sun, Interlayer-expanded MoS_2, Mater. Today 20 (2) (2017) 83–91, http://dx.doi.org/10.1016/j.mattod.2016.10.004.

[61] H. Li, Q. Zhang, C.C.R. Yap, B.K. Tay, T.H.T. Edwin, A. Olivier, D. Baillargeat, From bulk to monolayer MoS_2: Evolution of Raman scattering, Adv. Funct. Mater. 22 (7) (2012) 1385–1390, http://dx.doi.org/10.1002/adfm.201102111.

[62] R.N. Gontijo, A. Gadelha, O.J. Silveira, B.R. Carvalho, R.W. Nunes, L.C. Campos, M.A. Pimenta, A. Righi, C. Fantini, Temperature dependence of the double-resonance Raman bands in monolayer MoS_2, J. Raman Spectrosc. 50 (12) (2019) 1867–1874, http://dx.doi.org/10.1002/jrs.5736.

[63] H. Zeng, B. Zhu, K. Liu, J. Fan, X. Cui, Q.M. Zhang, Low-frequency Raman modes and electronic excitations in atomically thin MoS_2 films, Phys. Rev. B 86 (2012) 241301, http://dx.doi.org/10.1103/PhysRevB.86.241301.

[64] L. Li, Z. Qin, L. Ries, S. Hong, T. Michel, J. Yang, C. Salameh, M. Bechelany, P. Miele, D. Kaplan, M. Chhowalla, D. Voiry, Role of sulfur vacancies and undercoordinated Mo regions in MoS_2 nanosheets toward the evolution of hydrogen, ACS Nano 13 (6) (2019) 6824–6834, http://dx.doi.org/10.1021/acsnano.9b01583.

[65] W.M. Parkin, A. Balan, L. Liang, P.M. Das, M. Lamparski, C.H. Naylor, J.A. Rodríguez-Manzo, A.T.C. Johnson, V. Meunier, M. Drndić, Raman shifts in electron-irradiated monolayer MoS_2, ACS Nano 10 (4) (2016) 4134–4142, http://dx.doi.org/10.1021/acsnano.5b07388.

[66] P. Maguire, C. Downing, J. Jadwiszczak, M. O'Brien, D. Keane, J.B. McManus, G.S. Duesberg, V. Nicolosi, N. McEvoy, H. Zhang, Suppression of the shear Raman mode in defective bilayer MoS_2, J. Appl. Phys. 125 (6) (2019) 064305, http://dx.doi.org/10.1063/1.5086366.

[67] Q. Wang, X. Li, X. Ma, Z. Li, Y. Yang, Activation of the MoS_2 basal plane to enhance CO hydrogenation to methane activity through increasing S vacancies, ACS Appl. Mater. Interfaces 14 (6) (2022) 7741–7755, http://dx.doi.org/10.1021/acsami.1c18291.

[68] X. Zhang, S. Wang, C.-K. Lee, C.-M. Cheng, J.-C. Lan, X. Li, J. Qiao, X. Tao, Unravelling the effect of sulfur vacancies on the electronic structure of the MoS_2 crystal, Phys. Chem. Chem. Phys. 22 (38) (2020) 21776–21783, http://dx.doi.org/10.1039/c9cp07004d.

[69] H. Fei, R. Liu, J. Wang, T. Guo, Z. Wu, D. Wang, F. Liu, Targeted modulation of competitive active sites toward nitrogen fixation via sulfur vacancy engineering over MoS_2, Adv. Funct. Mater. 33 (36) (2023) http://dx.doi.org/10.1002/adfm.202302501.

[70] Q. Liu, Q. Fang, W. Chu, Y. Wan, X. Li, W. Xu, M. Habib, S. Tao, Y. Zhou, D. Liu, T. Xiang, A. Khalil, X. Wu, M. Chhowalla, P.M. Ajayan, L. Song, Electron-doped 1T-MoS_2 via interface engineering for enhanced electrocatalytic hydrogen evolution, Chem. Mater. 29 (11) (2017) 4738–4744, http://dx.doi.org/10.1021/acs.chemmater.7b00446.

[71] W. Li, J. Huang, B. Han, C. Xie, X. Huang, K. Tian, Y. Zeng, Z. Zhao, P. Gao, Y. Zhang, T. Yang, Z. Zhang, S. Sun, Y. Hou, Molten-salt-assisted chemical vapor deposition process for substitutional doping of monolayer MoS_2 and effectively altering the electronic structure and phononic properties, Adv. Sci. 7 (16) (2020) 2001080, http://dx.doi.org/10.1002/advs.202001080.

[72] R. Zhang, L. Wei, J. Zhang, Y. Wang, X. Qiao, Y. Han, J. He, G. Zhang, X. Wu, L. Gu, S. Du, S.T. Pantelides, H.J. Gao, Superconductivity in potassium-doped metallic polymorphs of MoS_2, Proc. Natl. Acad. Sci. 113 (31) (2016) 8762–8765, http://dx.doi.org/10.1073/pnas.1606042113.

[73] Q. Li, Y. Zhang, W. Chen, J. Sun, W. Huang, H. Zhang, Intermediate phases in sodium intercalation into MoS_2 nanosheets, Nano Energy 38 (2017) 342–349, http://dx.doi.org/10.1016/j.nanoen.2017.06.024.

[74] M.D. Curtis, J.E. Penner-Hahn, K.E. Dungey, Alkali-metal intercalation of MS_2: structure and bonding, RSC Adv. 4 (2014) 2942–2953, http://dx.doi.org/10.1039/C3RA45477C.

[75] M. Tosun, L. Chan, M. Amani, T. Roy, G.H. Ahn, P. Taheri, C. Carraro, J.W. Ager, R. Maboudian, A. Javey, Air-Stable n-Doping of WSe_2 by Anion Vacancy Formation with Mild Plasma Treatment, ACS Nano 10 (7) (2016) 6853–6860, http://dx.doi.org/10.1021/acsnano.6b02521.

[76] G. Barik, S. Pal, Defect induced performance enhancement of monolayer MoS_2 for Li- and Na-ion batteries, J. Phys. Chem. C 123 (36) (2019) 21852–21865, http://dx.doi.org/10.1021/acs.jpcc.9b04128.

[77] S. Kim, M.Y. Lee, S. Lee, S.-H. Jhi, Super low work function of alkali-metal-adsorbed transition metal dichalcogenides, J. Phys.: Condens. Matter. 29 (31) (2017) 315702, http://dx.doi.org/10.1088/1361-648x/aa79bd.

[78] Y.-X. Yu, Theoretical insights into surface-phase transition and ion competition during alkali ion intercalation on the Cu_4Se_4 nanosheet, Phys. Chem. Chem. Phys. 26 (2024) 323–335, http://dx.doi.org/10.1039/D3CP05423C.

[79] Y.-X. Yu, Sodium/potassium intercalation on the Cu_4S_4 nanosheet accompanied by a surface phase transition and their competition with protons, ACS Appl. Energy Mater. 6 (19) (2023) 10048–10060, http://dx.doi.org/10.1021/acsaem.3c01623.